Dual-band Observations of the Asymmetric Ring around CIDA 9A: Dead or Alive?

Daniel Harsono[1] , Feng Long[2,3,15] , Paola Pinilla[4] , Alessia A. Rota[5], Carlo F. Manara[6] , Gregory J. Herczeg[7] ,
Doug Johnstone[8,9] , Giovanni Rosotti[5,10,11] , Giuseppe Lodato[11] , Francois Menard[12] , Marco Tazzari[13] , and
Yangfan Shi[14]

[1] Institute of Astronomy, Department of Physics, National Tsing Hua University, Hsinchu 30013, Taiwan
[2] Lunar and Planetary Laboratory, University of Arizona, Tucson, AZ 85721, USA
[3] Center for Astrophysics | Harvard & Smithsonian, 60 Garden Street, Cambridge, MA 02138, USA
[4] Mullard Space Science Laboratory, University College London, Holmbury St Mary, Dorking, Surrey, RH5 6NT, UK
[5] Leiden Observatory, Leiden University, P.O. Box 9513, NL-2300 RA, Leiden, The Netherlands
[6] 1European Southern Observatory, Karl-Schwarzschild-Strasse 2, D-85748 Garching bei München, Germany
[7] Kavli Institute for Astronomy and Astrophysics, Peking University, Yiheyuan 5, Haidian Qu, 100871 Beijing, People's Republic of China
[8] NRC Herzberg Astronomy and Astrophysics, 5071 West Saanich Road, Victoria, BC, V9E 2E7, Canada
[9] Department of Physics and Astronomy, University of Victoria, 3800 Finnerty Road, Elliot Building, Victoria, BC, V8P 5C2, Canada
[10] School of Physics and Astronomy, University of Leicester, Leicester, LE1 7RH, UK
[11] Dipartimento di Fisica, Universitá degli Studi di Milano, Via Giovanni Celoria, 16, I-20133 Milano, MI, Italy
[12] Univ. Grenoble Alpes, CNRS, IPAG / UMR 5274, F-38000 Grenoble, France
[13] INAF-Osservatorio Astrofisico di Arcetri, L.go E. Fermi 5, I-50125 Firenze, Italy
[14] Department of Astronomy, Peking University, Yiheyuan 5, Haidian Qu, 100871 Beijing, People's Republic of China
Received 2022 September 7; revised 2023 October 10; accepted 2023 October 12; published 2024 January 11

Abstract

While the most exciting explanation of the observed dust asymmetries in protoplanetary disks is the presence of protoplanets, other mechanisms can also form the dust features. This paper presents dual-wavelength Atacama Large Millimeter/submillimeter Array observations of a large asymmetric dusty ring around the M-type star CIDA 9A. We detect a dust asymmetry in both 1.3 and 3.1 mm data. To characterize the asymmetric structure, a parametric model is used to fit the observed visibilities. We report a tentative azimuthal shift of the dust emission peaks between the observations at the two wavelengths. This shift is consistent with a dust trap caused by a vortex, which may be formed by an embedded protoplanet or other hydrodynamical instabilities, such as a dead zone. Deep high-spatial-resolution observations of dust and molecular gas are needed to constrain the mechanisms that formed the observed millimeter cavity and dust asymmetry in the protoplanetary disk around CIDA 9A.

1. Introduction

The Atacama Large Millimeter/submillimeter Array (ALMA) has uncovered the early stages of planet formation, with dust continuum observations that reveal rings, gaps, spiral arms, and asymmetric dust emission (e.g., ALMA Partnership et al. 2015; Andrews et al. 2018; Cazzoletti et al. 2018; Huang et al. 2018; Long et al. 2018; Cieza et al. 2021). These features may be signatures of embedded planets or hydrodynamical instabilities may create them (see the review by Bae et al. 2023) that are creating planetesimals. Prime examples of these cradles of planet formation have been transition (or cold) disks (Espaillat et al. 2014), disks with a deep millimeter central cavity that are typically attributed to the presence of young giant planets (e.g., Duffell & Dong 2015; Fung & Chiang 2016; Calcino et al. 2020). However, young giant planets have only been reported in three protoplanetary disks, PDS 70, AB Aur, and HD 169142 (Keppler et al. 2018; Müller et al. 2018; Currie et al. 2022; Hammond et al. 2023); deep observations of molecular gas show gas gaps and kinematics that may point to

indirect evidence of protoplanets (van der Marel et al. 2016; Dong & Fung 2017; Fedele et al. 2021; Stadler et al. 2023).

Large millimeter dust cavities, rings, and large-scale azimuthal dust asymmetries are attributed to dust trapping induced by pressure bumps (e.g., Klahr & Henning 1997; Pinilla et al. 2012). Dust particles marginally coupled to the gas tend to accumulate at the local pressure maxima of a protoplanetary disk (Weidenschilling 1977; Birnstiel et al. 2010). The growth of dust particles is enhanced inside the pressure trap, leading to the potential planetesimal formation (e.g., Youdin & Goodman 2005; Johansen et al. 2007; Drazkowska et al. 2023). While many mechanisms can generate the pressure bumps (Bae et al. 2023), they are often associated with young Jovian planets, regardless of whether or not the planets are directly observable (e.g., Ataiee et al. 2013; Espaillat et al. 2014; Dong et al. 2015; Francis & van der Marel 2020). The interaction between the young planet and the disk can launch a spiral arm that is detectable in the infrared through scattered light (e.g., Bae et al. 2016; Dong & Fung 2017; Benisty et al. 2023; Paardekooper et al. 2023). In such a scenario, the young planet is expected to carve a deep gap in the protoplanetary disk, leading to different gas and dust distributions, where a substantial amount of gas is removed in some cases. Hydrodynamical simulations show that the exact depletion factor depends on the number of planets, their orbital orientation, and the viscosity in the disk (e.g., Duffell & Dong 2015; Pinilla et al. 2022, Bae et al. 2023).

---

[15] NASA Hubble Fellowship Program Sagan Fellow.

Alternative scenarios for the formation of large inner cavities are a close binary (Artymowicz & Lubow 1994), photoevaporation (Matsuyama et al. 2003; Alexander & Armitage 2007), magnetohydrodynamic winds (Suzuki & Muto 2010), dead zones (Pinilla & Flock 2016; Delage et al. 2022), or a combination of these mechanisms (Rosotti et al. 2013; Gárate et al. 2021). Each proposed mechanism has observable features that can be tested against spatially resolved dust and gas observations, but there are degeneracies. For example, all of them are expected to trigger dust trapping at the outer edge of the cavity. Nonetheless, there are some distinct predictions for each of these mechanisms. For instance, an inner cavity formed by a dead zone may show a *radial* shift between different sizes of dust grains that is dissimilar from the planet–disk interaction models. In the dead zone case, the location of the radial peak is closer at longer wavelengths (tracing larger grains) than at short wavelengths (tracing smaller grains; Figure 5 in Pinilla et al. 2019). This difference can be tested by observing dust emission at two frequencies within the ALMA bands. On the one hand, a vortex generated by a planet(s) inside the cavity will create an observable azimuthal shift in the dust millimeter emission (Baruteau & Zhu 2016), while it is still unclear if that is the case in the dead zone case. On the other hand, disk winds can be detected through broad (>5 km s^{-1}) molecular and atomic lines (e.g., Pascucci et al. 2011; Klaassen et al. 2013, 2016; Booth et al. 2021). Therefore, with high-spatial-resolution observations of gas and dust emission at different wavelengths, it is possible to start ruling out one or more of the proposed mechanisms toward specific systems.

Thus far, a few disks show a clear azimuthal asymmetry in the millimeter dust emission. Protoplanetary disks around IRS48 (van der Marel et al. 2013) and HD142527 (Casassus et al. 2013) are iconic examples of azimuthally asymmetric dust disks revealed by ALMA. Other disks show various dust substructures, such as a dust ring morphology (Kraus et al. 2017; Boehler et al. 2018; Liu et al. 2019) or large horseshoe-like shape (Tang et al. 2012; Cazzoletti et al. 2018; Muro-Arena et al. 2020; van der Marel et al. 2021). By spatially resolving the disk around HD135344B, Cazzoletti et al. (2018) reported an azimuthal shift between observations at different wavelengths toward its dust arc, indicating a vortex. Recently, Boehler et al. (2021) also demonstrated how deep observations of molecular lines can be used to study the kinematics around a large vortex in HD142527.

Most previous detections and characterizations of large azimuthal asymmetries have been found toward protoplanetary disks around Herbig stars. In the Taurus disk survey by Long et al. (2018), the disk around the M2 primary star CIDA 9A shows a $\sim$25 au inner cavity and an asymmetric dust ring. CIDA 9 (BCG93 9; Briceno et al. 1993) is a binary system with a separation of 2″35 (Manara et al. 2019), which corresponds to a projected separation of 411 au at a distance of 175 pc (Gaia Data Release 3, or DR3; Gaia Collaboration et al. 2021). The central star has a lower mass than the other systems whose disks show a large millimeter cavity, providing a test for disk evolution around lower-mass stars where dust radial drift is expected to be more efficient. Although still not well studied, the general properties of disks around very low-mass stars tend to follow their solar-mass star counterparts (Kurtovic et al. 2021). For example, the detection of a 20 au cavity around the M 4.5 star CIDA 1 suggests that a Saturn-mass planet is needed to open the gap (Pinilla et al. 2018).

We obtained ALMA dual-band observations of the disk around CIDA 9A to better understand the origin of its large millimeter cavity and asymmetric dust disk. In this paper, we report on the detection of a large-scale azimuthal asymmetric ring in both Bands 3 (3.1 mm) and 6 (1.3 mm) around the primary star CIDA 9A, with an azimuthal shift in the asymmetry between the two wavelengths. This paper is organized as follows. Section 2 describes the observational details and the synthesis imaging. The dust continuum and gas observations analysis can be found in Section 3. We discuss the implications of the observed substructures in the context of a vortex and its lifetime in Section 4. Finally, Section 5 summarizes the paper and the conclusions.

2. Observational Details

2.1. CIDA 9A Stellar Properties: Mass and Age

The stellar mass and age estimates of CIDA9A are obtained by comparing the stellar isochrone to the stellar luminosity and temperature. Based on fitting the photosphere, accretion, and extinction to low-resolution optical spectra, CIDA 9A has a spectral type of M1.8 ($T_{\rm eff} = 3592$ K and a luminosity of 0.21 $L_\odot$; Herczeg & Hillenbrand 2014), after accounting for an extinction $A_V = 1.35$, contribution from accretion, and being corrected for $d = 175$ pc (Gaia Collaboration et al. 2021). The automated temperature measured from LAMOST spectra of 3675 K is slightly higher (Luo et al. 2019), perhaps because the fit to the LAMOST spectra did not include an accretion component. A similar luminosity is retrieved when using PAN-STARSS y- and z-band photometry (Chambers et al. 2016) and color and bolometric corrections by Pecaut & Mamajek (2013) and Zhou et al. (2022).

These parameters lead to a mass of $\sim$0.42 $M_\odot$ and age of 3.5 Myr, when compared to standard evolutionary models (Baraffe et al. 2015; Somers et al. 2020, without spots) and a mass of $\sim$0.66 $M_\odot$ and age of $\sim$6 Myr for models that include nonstandard physics (the magnetic models of Feiden 2016 or the models from Somers et al. 2020 with 50% spot coverage). If the stellar mass is $\gtrsim$0.7 $M_\odot$, the stellar age would be as high as 6–10 Myr. However, the radius may be underestimated if the star is heavily spotted, which can lead to an overestimation of the effective temperature for the visible surface (Gully-Santiago et al. 2017). The brightness of CIDA 9A varies from $V = 15$ to 17 mag in ASAS-SN monitoring (Shappee et al. 2014; Kochanek et al. 2017), which also introduces significant uncertainties in any radius estimate.

While most of the Taurus young stellar objects are at a distance of 130–200 pc (Galli et al. 2019; Krolikowski et al. 2021) and ages between 1 and 3 Myr, there are some apparent outliers and older subclusters with ages up to $\sim$20 Myr (Kraus et al. 2017; Krolikowski et al. 2021; Liu et al. 2021). It seems plausible that CIDA 9 is an old system in the Taurus Molecular Cloud, although age estimates are uncertain on any individual star (see the uncertainties described by Soderblom et al. 2014), especially one with such high amplitude variability.

The accretion luminosity of 0.026 $L_\odot$ is measured from the excess hydrogen continuum emission in a flux-calibrated optical spectrum that covers the Balmer Jump (from the spectrum described in Herczeg & Hillenbrand 2014 and following the methods described in Herczeg & Hillenbrand 2008). This accretion luminosity corresponds to an accretion rate of

Table 1
Targeted Spectral Windows in Band 3 and Molecular Lines

Spectral Window	ν_0 (GHz)	$d\nu$ (kHz)	dv (km s^{-1})	Transitions
1	97.976	61.035	0.19	CS2 − 1
2	97.695	61.035	0.19	⋯
3	95.999	976.562	3.0	⋯
4	109.777	61.035	0.17	C^{18}O1 − 0
5	110.196	61.035	0.17	^{13}CO1 − 0
6	107.894	976.562	2.7	⋯

Table 2
Properties of the Compact Dust Continuum Emission at 93 and 233 GHz

Name	Beams (arcsec, arcsec, deg)	rms (mJy bm^{-1})	S_ν (Jy)	$I_{\nu,\mathrm{peak}}$ (mJy bm^{-1})
		Briggs 0.5		
Band 3	0.14, 0.05, 3.7	0.02	1.8 ± 0.4	0.3
Band 6	0.13, 0.10, 2.2	0.1	34 ± 6	2.8
		Briggs 0.5, Taper at 0″09		
Band 3	0.135, 0.135, 0	0.03	2.6 ± 0.6	0.4
Band 6	0.135, 0.135, 0	0.07	34 ± 6	3.5

Note. Flux densities (S_ν) are calculated in the image plane by summing up the pixels with $I_\nu > 3\sigma$.

1.8×10^{-9} $M_\odot$ yr^{-1}, for the adopted parameters 1.18 $R_\odot$ and 0.66 $M_\odot$.

2.2. ALMA Observations

ALMA observed CIDA 9A on 2021 July 9 during the Return to Operations phase. The number of antennas in operation was 38. A few antennas among the 38 showed an elevated temperature during atmospheric calibration. The data were calibrated with the CASA (McMullin et al. 2007) pipeline, version 2021.2.0.128, with CASA 6.2.1.7. Two antennas were flagged out and ~10% of the data toward the phase calibrator were flagged. Despite a number of issues during calibration, the data were deemed science-ready.

CIDA 9 was observed in Band 3 using six spectral windows, as shown in Table 1. The main targeted lines are C^{18}O $J = 1-0$ (109.7822 GHz, $E_{\mathrm{up}}/k_B = 5.27$ K, $\log_{10}(A_{\mathrm{ul}}) = -7.203$), ^{13}CO $J = 1-0$ (110.2014 GHz, $E_{\mathrm{up}}/k_B = 5.29$ K, $\log_{10}(A_{\mathrm{ul}}) = -7.198$), and CS $J = 2-1$ (97.2710 GHz, $E_{\mathrm{up}}/k_B = 7.05$ K, $\log_{10}(A_{\mathrm{ul}}) = -4.77$). The properties of the molecular transitions are obtained from the CDMS (Müller et al. 2005; Endres et al. 2016) and JPL (Pickett et al. 1998) catalogs. The range of baselines was 122 m to 12.6 km. The data were finally imaged and self-calibrated using the latest CASA 6.4. The phase center of the Band 3 data is International Celestial Reference System 05:05:22.821 + 25:31:30.426. A single-phase self-calibration was performed using the aggregate pseudocontinuum. The images were cleaned using the TCLEAN task in standard mode with a Briggs (Briggs 1995) weighting of 0.5. The final images and their noise levels are tabulated in Table 2.

The spectral lines were imaged after continuum subtraction via UVCONTSUB. Due to the flux uncertainties of the phase calibrator and the high fraction of flagging, we adopt a 20% flux uncertainty in Band 3 observations throughout this paper. We have combined our data with published Band 6 observations (Long et al. 2018; Manara et al. 2019; Rota et al. 2022). The Band 6 data were corrected for the proper motion of CIDA 9A using the Gaia DR2 data (Gaia Collaboration et al. 2018; Lindegren et al. 2018).

3. Results

3.1. Dust Continuum Emission around the Primary

In order to compare the Band 3 and Band 6 images, the images are deconvolved, including a (u, v) tapering at 0″09 and a common 0″135 beam, to restore the final image. These tapered images are shown in Figure 1. The original images at their respective native resolution are shown in Appendix A.

First, we analyze the data in the image plane to detect any radial and azimuthal shifts between Bands 3 and 6. There are two dust concentrations: the main bright dust emission peak on the east side (hereafter, the main dust emission peak) and the fainter localized arc to the west (hereafter, the secondary peak). The main dust emission peak in Band 3 seems aligned with the Band 6 image. The deprojected dust emission profiles are plotted in Figure 2, using the inclination and position angles found in Section 3.2. Long et al. (2018) found that the ring is located at a deprojected distance of 0″23, corresponding to 40 au (updated for the new Gaia DR3 distance). The main peak seems to lie within the ring, without any noticeable radial shifts between the two observations. The secondary peak to the west seems to indicate a radial extension up to ~0″2 with respect to Band 6, which is more than a single beam across.

An asymmetric dust continuum emission is observed at 96 GHz (3.1 mm), similar to that seen in the Band 6 data (1.3 mm; Long et al. 2018). The emission at the east side of the disk is brighter by 16%, with a significance level of 2.3σ, than the west side of the disk. The north and south variation is 33% in Band 3, which is ~3σ, while it is 29% in Band 6 (~13σ). In addition, the south side is brighter than the north side. Our new Band 3 image shows more pronounced asymmetries in the east–west and north–south directions. More of the dust emission in the ring is concentrated on the southeast side of CIDA 9A. CIDA 9A's companion, CIDA 9B, is not detected in Band 3 (see Appendix A). Here, we focus on the disk around the primary star CIDA 9A.

The dust grain distribution is usually estimated from the dust spectral index. If the dust emission is optically thin, the multifrequency dust spectral index α ($S_\nu \propto \nu^\alpha$) should be smaller than 3 to indicate the presence of larger dust grains (with caveats as discussed by Testi et al. 2014). To infer the dust grain population around the dust emission peaks, we need to understand the relationship between dust emission, the dust optical depth, and the dust spectral index (e.g., Carrasco-González et al. 2019). In general, the dust emission is given by

$$I_\nu = B_\nu(T_{\mathrm{dust}})[1 - \exp(-\tau)], \tag{1}$$

where τ is the dust optical depth and B_ν is the Planck function for a given dust temperature T_{dust}. The dust temperature profile is approximated as a power law following the irradiated flared disk model of Kenyon & Hartmann (1987):

$$T_{\mathrm{dust}}(R) = T_\star \left(\frac{R_\star}{R}\right)^{1/2} \phi_{\mathrm{flaring}}^{1/4}, \tag{2}$$

where ϕ is the flaring angle of 0.05 (Dullemond & Dominik 2004), a stellar temperature $T_\star$ of 3592 K, and a stellar radius $R_\star$ of ~1.2 $R_\odot$ (values are obtained from Herczeg & Hillenbrand 2014, adjusted to a distance of 175 pc). The dust
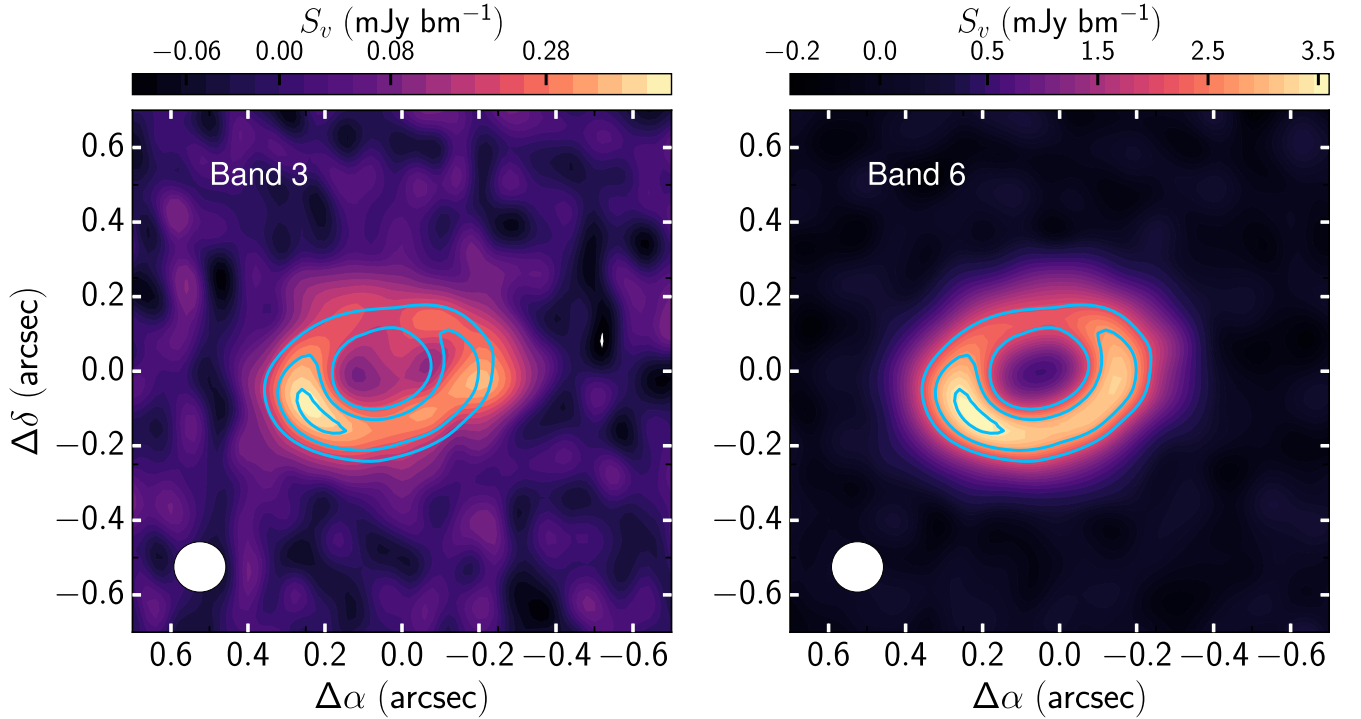
Figure 1. Dust continuum emission toward CIDA 9A in both Bands 3 (left) and 6 (right). The images are deconvolved using a tapering at $0''09$ and are restored with a $0''135 \times 0''135$ beam. The blue contour lines indicate the 30σ, 40σ, and 50σ levels of the Band 6 image, to highlight the difference in the dust continuum peaks. The peak position in Band 3 is shifted clockwise with respect to the peaks seen in Band 6. The noise levels are tabulated in Table 2.
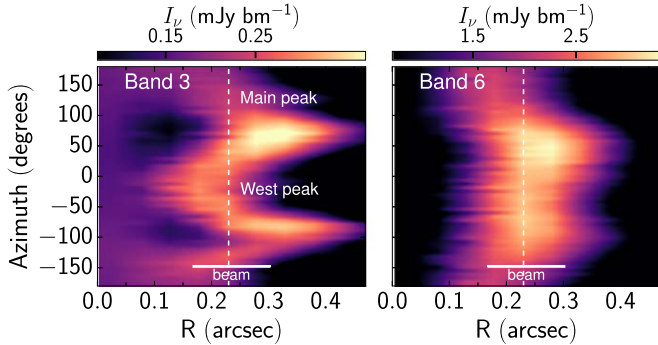
Figure 2. Profile of the dust emission in Bands 3 (left) and 6 (right). The vertical dashed line ($R = 0''23$) shows the location of the emission peaks in Band 6, which corresponds to the dust ring location of Long et al. (2018). The color scale is stretched differently with respect to Figure 1 to highlight the dust emission peaks. The coordinates have been deprojected using the inclination and position angle obtained in Section 3.2.

optical depth depends on the surface mass density of the dust and the total dust extinction $\chi_\nu = \kappa_{abs} + \sigma_{sca}$. For simplicity, we consider dust emission from the dust-absorption-dominated region. In this limit, the dust emission is given by

$$I_\nu = B_\nu(T_{dust})[1 - \exp(-\tau_0(\nu/\nu_0)^\beta)], \qquad (3)$$

with the dust absorption opacity slope β. At the location of the ring, the dust temperature is ≈ 25 K and the dust spectral index $\alpha = \log(I_{\nu_1}/I_{\nu_2})/\log(\nu_1/\nu_2)$. Only in the case where $\tau_{dust} < 1$ can we estimate the particle size distribution from α, and the dust spectral index should be $\alpha \approx \beta + 2$. As τ_{dust} approaches 1, α approaches 2. In general, α is ~ 3.7 for interstellar medium dust grains and is $2 \sim 3$ if the dust grains have grown to larger sizes, as $\alpha < 2$ could indicate nonthermal emission

contribution. The exact value depends on the composition and size distribution of the dust grains (Testi et al. 2014).

To estimate the dust optical depth, we compare the observed intensity with the expected dust emission, such that $T_{brightness} = T_{dust}(1 - e^{-\tau_\nu})$, while considering that the dust emission is evenly distributed within the beam. The average brightness temperatures around the two dust emission peaks are 3–5 K. Using the expected dust temperature of 25 K, the optical depth in Band 3 is $\tau_{B3} \sim 0.1$, while it is $\tau_{B6} \sim 0.3$ in Band 6 within a $0''135$ beam. The typical error in τ is <0.1, depending on the adopted temperature (15–25 K) and 10% error on the brightness temperature. At the native resolution, the optical depth increases by a factor of 2, indicating that the dust ring is still unresolved. Therefore, the observed dust emission in Band 3 can be considered optically thin for this analysis, while the dust emission in Band 6 is marginally optically thick, after considering the beam filling factor, since the optical depth approaches 0.5 within a $0''135$ beam.

We directly calculate the dust spectral index α_{B6-B3} in the image plane by evaluating $\log(I_{B3}/I_{B6})/\log(\nu_{B3}/\nu_{B6})$. The value α_{B6-B3} is evaluated using pixels with intensities $>5\sigma$ in both the Band 3 and 6 images. Figure 3 shows the dust spectral index profile along the two dust emission peaks. As a check, we also determined the spectral index from the concatenated observations. To construct the spectral index, we first align the Band 3 and 6 data using FIXPLANETS. The concatenated visibilities are deconvolved using TCLEAN with the Multi-term Multi-Frequency Synthesis (MTMFS) with three Taylor coefficients (Tsukagoshi et al. 2022). These images and comparisons to the values evaluated in the image plane are shown in Appendix A. For the purpose of this paper, we will present the spectral index values calculated from the images in Figure 1.

As shown in Figure 3, the localized lower spectral index of $\alpha_{B6-B3} \sim 2.8$ is found near the main dust peak, while the
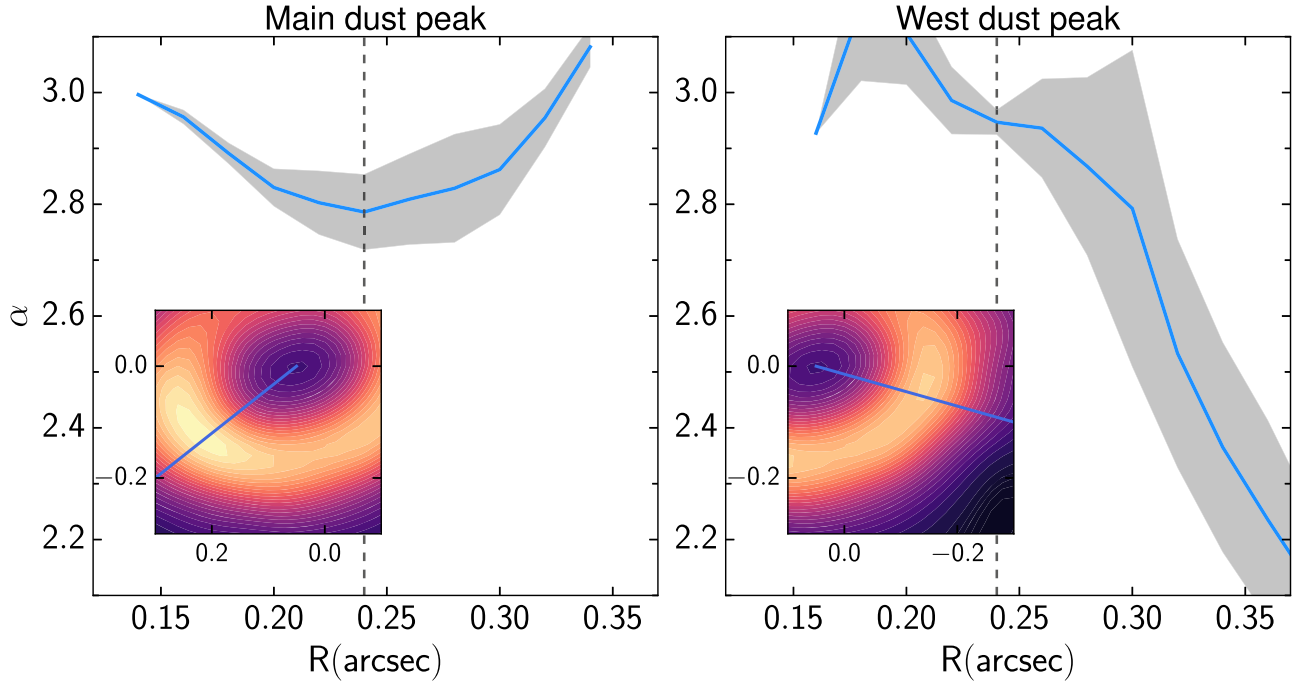
Figure 3. Dust spectral index profile of the dust emission peaks to the east (main, left) and west (right). We plot the mean α values within a beam as a function of distance from the center in arcseconds in blue, while the gray-shaded regions indicate the dispersion around the mean. The vertical dashed lines are placed at the rough locations of the peaks. The insets show the zoom-in view to the emission peak that is associated with each panel, along with the radial cut that is shown by the blue line. The color scale in the insets is similar to Figure 1.

secondary peak shows an averaged $\alpha_{\rm B6-B3}$ of 2.9. The standard flux uncertainty produced by the ALMA pipeline tends to be poorer than 10% (Francis et al. 2020). However, our Band 3 observations were taken during the return to operations phase, which may lead to higher flux uncertainty, as inferred from the large phase rms. The typical error of the spectral index is 0.2 (10% flux uncertainty) and 0.3 (20% flux uncertainty). Despite the possible flux calibration issues, the major uncertainty lies in the parameters chosen during the image reconstruction using TCLEAN. Depending on the parameters used during the deconvolution, the spectral index can vary by 0.5. Nevertheless, a lower spectral index is found for the main dust emission peak with $\alpha < 3$. Note that the images are deconvolved using a taper and a common beam. The actual dust spectral index of the ring itself is a lower value if we use the images at their native resolution with higher noise levels.

3.2. (u, v) Modeling of the Dust Morphology around CIDA 9A

By fitting the (u, v) data, we can accurately determine the location of the observed dust peaks in Bands 3 and 6, such that any azimuthal and radial shifts can be measured by comparing the best-fit parameters. We fit the data with morphological models using *Galario* (Tazzari et al. 2018). First, following Long et al. (2018), the data are fit with an axisymmetric Gaussian ring,

$$I_{\rm Ring}(r) = A \exp\left[-\frac{(R - R_0)^2}{2\sigma^2}\right], \qquad (4)$$

where the ring is centered at R_0 with a Gaussian width of σ. We confirm that the results of our fits to the Band 6 data are identical to Long et al. (2018), which are listed in Table 3 (see Appendix C).

Table 3
Location of the Dust Peaks from the (u, v) Fitting

| B	R_0 (au)	$R_{\rm arc}$ (au)	θ_1 (deg)	θ_2 (deg)	i (deg)	PA (deg)
	Symmetric Gaussian Ring					
3	42^{+1}_{-1}	...	...	...	48.6^{+1}_{-1}	99.5^{+1}_{-1}
6	40^{+2}_{-2}	...	...	...	$45.9^{+0.2}_{-0.1}$	$104^{+0.2}_{-0.2}$
	Symmetric Gaussian Ring + Two Arcs					
3	42^{+1}_{-1}	$40^{+0.2}_{-0.2}$	36^{+20}_{-16}	122^{+20}_{-18}	48^{+1}_{-1}	97^{+2}_{-1}
6	$42^{+0.2}_{-0.2}$	$37^{+0.2}_{-0.2}$	58^{+3}_{-2}	146^{+10}_{-19}	$45^{+0.5}_{-1}$	$110^{+0.8}_{-4}$

To recover any nonaxisymmetric dust emission around CIDA 9A, we proceed to employ an asymmetric azimuthal Gaussian ring (hereafter, arc model) in addition to the axisymmetric Gaussian ring intensity model. The arc model is based on a description of a vortex in a protoplanetary disk by Lyra & Lin (2013; see also Cazzoletti et al. 2018). This particular model creates the arc feature $I_{\rm ARC} = I_1 + I_2$, where

$$I_1(r, \theta) = A \exp\left[-\frac{(R - R_{\rm arc})^2}{2\sigma_r^2}\right] \exp\left[-\frac{(\theta - \theta_1)^2}{2\sigma_{\theta_1}^2}\right] \qquad (5)$$

and

$$I_2(r, \theta) = A \exp\left[-\frac{(R - R_{\rm arc})^2}{2\sigma_r^2}\right] \exp\left[-\frac{(\theta - \theta_2)^2}{2\sigma_{\theta_2}^2}\right], \qquad (6)$$

respectively, with I_1 describing the intensity profile clockwise with respect to the center of the arc θ_1 ($\theta < \theta_1$, 0° is east) and I_2 is the intensity profile counterclockwise of θ_2 located at the radius $R_{\rm arc}$. The model creates arc-like features by separating
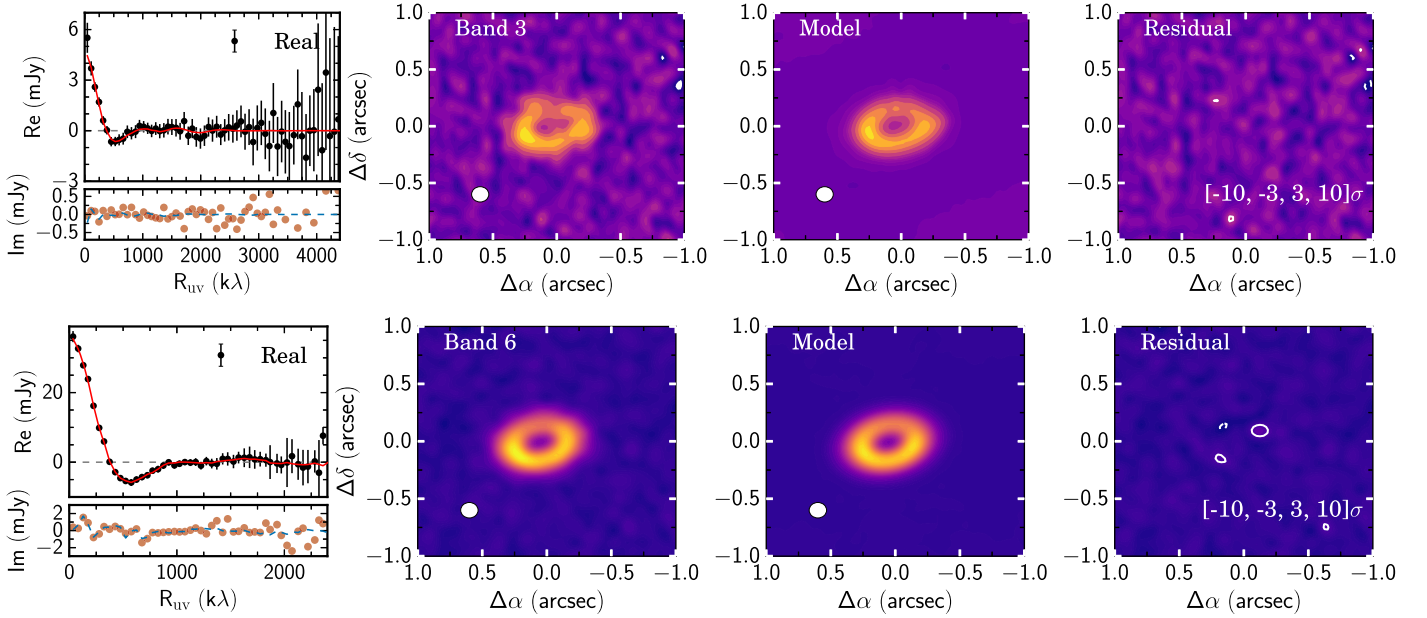
Figure 4. Best-fit symmetric Gaussian ring and two asymmetric Gaussian ring (GR2ARC) models for both Bands 3 and 6. Top: the best-fit models for the Band 3 data. Bottom: the best-fit models for the Band 6 data. For each row, we show the binned visibilities, the original image, the model image, and the residual. For the residual image, the contours at -10σ, -3σ, 3σ, and 10σ are indicated by the white lines.

the east and west sides of the Gaussian ring. The free parameters are the intensity A, radial position of the arc R_{arc}, width in radial direction σ_r, angular position θ_1 or θ_2, where the arc corresponds to I_1 and I_2, width in the position angle directions σ_{θ_1} and σ_{θ_2}, position angle PA, inclination i, and offset from the phase center ($\Delta\alpha$, $\Delta\delta$). The total model is the symmetric Gaussian ring and two asymmetric Gaussian ring models (arcs), such that $I_{total} = I_{Ring} + I_{ARC1} + I_{ARC2}$ (hereafter GR2ARC). For this paper, we have fixed the location of the arcs at a single R_{arc}. In total, we have 18 free parameters.

The best-fit parameters are determined using *Galario* and the *emcee* packages (Foreman-Mackey et al. 2013) to explore the parameter space efficiently. For each model, Gaussian and GR2ARC, we performed 10,000 steps with a burn-in that is determined through the autocorrelation function (~1500–2000 steps). From these runs, the best-fit parameters are determined statistically using steps with an acceptance fraction of 0.2. We report the mean of the parameters, and their errors are calculated from the standard deviation from the mean. We subtract the modeled visibilities from the observations using these best-fit values to create the residual maps. The best-fit model and residual maps are shown in Figures 4 and 13 (in Appendix C) for the GR2ARC and Gaussian models, respectively. The best-fit values are listed in Table 3. The models capture most of the observed features with 1σ–3σ residuals, as seen from the last panels in Figures 4 and 13. These residuals are minimized by the GR2ARC model, as shown in Figure 4.
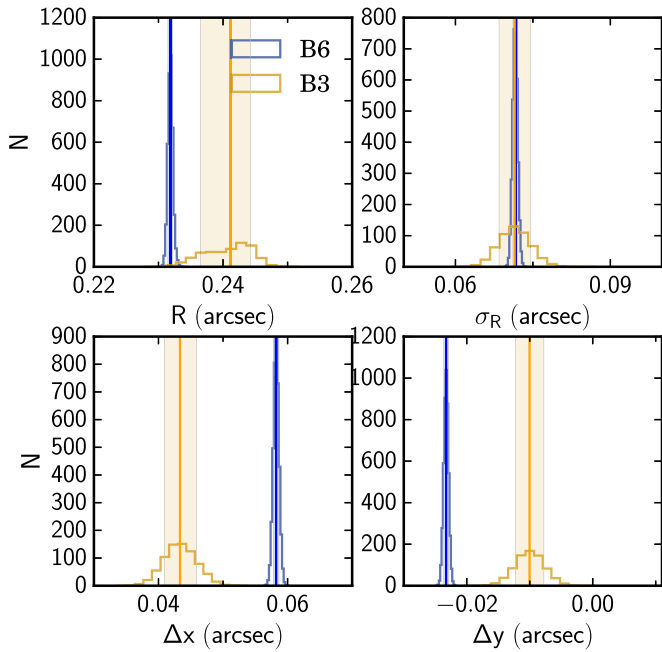
The axisymmetric Gaussian ring model indicates that the ring in Band 3 is radially shifted by 0″01 or 2 au with an error ~2 au with respect to the Band 6 visibilities. The center of the observations is determined with uncertainties of ~0″01. Considering these uncertainties, the rings in Bands 3 and 6 are located at the same radius based on the axisymmetric Gaussian models. We will then focus on the best-fit parameters of the GR2ARC model. Table 3 shows the best-fit parameters with restricted locations for the axisymmetric Gaussian ring
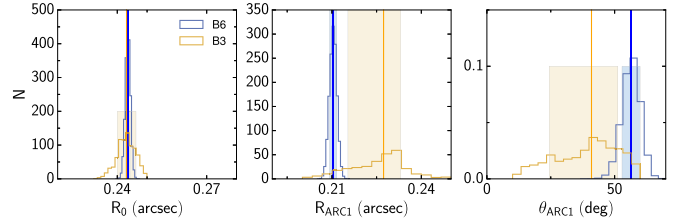
Figure 5. Comparison between the best-fit values of the GR2ARC model in Bands 3 and 6. The main parameters of the ring and the main arc are shown for simplicity. The mean and standard deviation for each of the parameters are plotted after taking into account the burn-in phase (~2000) and an acceptance rate of 15%. The Band 6 results are shown in blue, while the Band 3 results are shown in orange.

and arcs. If we let the radial location R be free, the center of the ring (R_0) is located at 44 ± 1 au for Band 6, while it is 44^{+7}_{-6} au in Band 3. The main dust peak is fitted with the arc located at 37 ± 0.2 au in Band 6, while it is at 40 ± 0.6 au in Band 3. Similarly, the center position of the two observations is fitted with statistical uncertainties of ~1–2 au (see Figures 5 and 6). Considering the uncertainties in the center position and proper motion, we report an upper limit to the radial shift $\lesssim 3$ au between Bands 3 and 6.

The main dust peak shows an azimuthal shift between Bands 3 and 6. The peak in Band 3 is located at 36^{+20}_{-16} °, while the Band 6 data are centered at 58^{+3}_{-2} °, which results in a 22^{+5}_{-36} ° shift (see Figure 5). We fit the observed visibilities twice using the GR2ARC model. The first run allows all of the parameters, including the position of the arc R_{arc}, to be free, which implies that I_1 can be radially shifted with respect to I_2. The second set of runs restricts the arcs, I_1 and I_2, to be at the same radius R_{arc}. In comparison, without restricting the radial locations of the ring and the two arcs (the first set of runs), the angular difference is ~80°. Meanwhile, the location of the second arc that describes the west peak is similar in both Bands 3 and 6. With this (u, v) modeling, we find a tentative azimuthal shift in the main dust peak between Bands 3 and 6, since the shift is

Figure 6. Similar to Figure 5, but for the axisymmetric Gaussian ring models.

seen in Figure 2 and recovered through the visibilities analysis with non-negligible uncertainties. We calculated the Bayesian information criterion (BIC) for each of the intensity models, which is given by $n_{par} \log N_{data} - 2 \log \mathcal{L}_{max}$, where n_{par} is the number of parameters, N_{data} is the number of data points, and $\mathcal{L}_{max}$ is the maximum likelihood function of the model given the best-fit parameters. Even though the GR2ARC model returns a lower residual map in Band 6 (see Figure 4), its BIC value is much greater than the Gaussian ring model by a factor of 3. This implies that we cannot conclusively determine that GR2ARC is the better model for the observations presented here.

Using these models, we constructed the model images within CASA to determine the spectral index. The dust spectral index α obtained from the model images is ∼2.6–2.9 at the dust continuum peaks. These values are consistent with the observed dust spectral index in Figure 3. Using the models, we can further estimate the dust spectral index of the dust ring itself without deconvolution. The underlying intensity models indicate that the spectral index at the main dust peak is ∼2. The optical depth of the best-fit images shows that $\tau_{B6} = 2$ while $\tau_{B3} \sim 0.4$. Therefore, the models indicate that the main dust peak is optically thick with a low spectral index.

3.3. Molecular Line Emission

Along with the dust continuum, the Band 3 observations also targeted ^{13}CO $J = 1$–0 (110.2014 GHz), $C^{18}O$ $J = 1$–0 (109.7822 GHz), and CS $J = 2$–1 (97.2710 GHz). We have also included the ^{13}CO $J = 2$–1 and $C^{18}O$ $J = 2$–1 observations from Manara et al. (2019) and Rota et al. (2022) for completeness. We have used a Keplerian masking, using the parameters of Rota et al. (2022; $i = 56°$, PA=284.2°), to extract the molecular lines in Bands 3 and 6 using *GoFish* (Teague 2019). Figure 7 shows the integrated line emission from the primary disk. We detect the weak ^{13}CO 1–0 and $C^{18}O$ 1–0 emissions using the Keplerian mask. The low-J lines suffer

Table 4
Comparison of the Integrated Line Flux Densities in Jy km s^{-1}

| Source	^{13}CO 1–0	^{13}CO 2–1	$C^{18}O$ 1–0	$C^{18}O$ 2–1
Rota+22	⋯	$0.49^{+0.02}_{-0.02}$	⋯	$0.12^{+0.01}_{-0.01}$
1″5	<0.08	0.51 ± 0.14	<0.1	0.32 ± 0.15
0″5	0.030 ± 0.01	0.23 ± 0.03	0.04 ± 0.02	0.10 ± 0.01

Note. Rota et al. (2022) reported the total fluxes obtained from their cumulative flux technique. We report the total integrated flux density inside 1″5 and 0″5 circles using *GoFish*, adopting a 20% error.

from foreground absorption. Meanwhile, both SO$_2$ and CS line emissions are tentatively detected.

Since the velocity-based masking is able to extract the disk emission, we proceed to fit the $J = 2$–1 line with *eddy* (Teague 2019). For our fitting, we fix the inclination to $i = 47° \pm 2°$, based on the orientation of the dust disk in Section 3.2. The dust disk and gas disk as observed from the rotational transitions in the submillimeter should not be strongly misaligned, hence we adopt the inclination of the dust disk. The first moment maps are obtained using *bettermoments* (Teague & Foreman-Mackey 2018), with the quadratic method including a 3σ clip. The first moment maps are fitted using *eddy* with 2000 steps, including a 10% burn-in. We obtain a stellar mass of 0.62 $M_\odot$ using the ^{12}CO 2–1 line and 0.72 $M_\odot$ with the ^{13}CO 2–1 line. The typical error on the stellar mass is <0.1 $M_\odot$. If we adopted an inclination of 56° instead (Rota et al. 2022), emission models would provide a better fit to the high-spatial-resolution CO lines, as obtained along with the data presented in Long et al. (2018), but a worse fit with larger residuals in the short-baseline data presented here. With the longer-baseline configuration, a significant part of the line emission at 3–5 km s^{-1} is not recovered. For the purpose of this paper, we adopt the lower-inclination fit solution with a stellar mass between 0.62 and 0.72 $M_\odot$, an inclination of $47° \pm 2°$, and a position angle between 277° and 283°.

Using these parameters, we integrate the $J = 1$–0 and $J = 2$–1 lines of ^{13}CO and $C^{18}O$. The molecular line emission is detected between 2 and 10 km s^{-1}. The integrated line flux density is calculated by integrating the line profile obtained with *GoFish* with the maximum radius of 1″7 obtained by Rota et al. (2022). The velocity range for the integration is estimated from the line profiles as shown in Figure 7. For the weak lines CS and SO2, the line emission is integrated from 4 to 10 km s^{-1}, where the tentative SO2 line is seen. For the ^{13}CO $J = 2$–1 lines, the total integrated flux density is derived using the images from Rota et al. (2022). The error is given by the number of channels and the rms, such that $1.2 \times \sqrt{N_{chan}} \times$ rms. The first factor of 1.2 considers the 20% flux uncertainty. Note that the ^{13}CO $J = 2$–1 lines presented in Rota et al. (2022) are obtained with a shorter-baseline configuration than the data presented in Long et al. (2018).

By adopting a higher stellar mass, the integrated line flux density and the peak intensity of ^{13}CO 1–0 and SO$_2$ are higher by more than 20% (see Table 4 for comparison). These data support a stellar mass for CIDA 9A of at least 0.6$M_\odot$. Unfortunately, the data are not deep enough to search for any kinematical disturbances within the millimeter cavity. Due to the low signal-to-noise ratio (S/N) of the gas-line observations, we do not detect any broad molecular line emission that can be

Harsono et al.
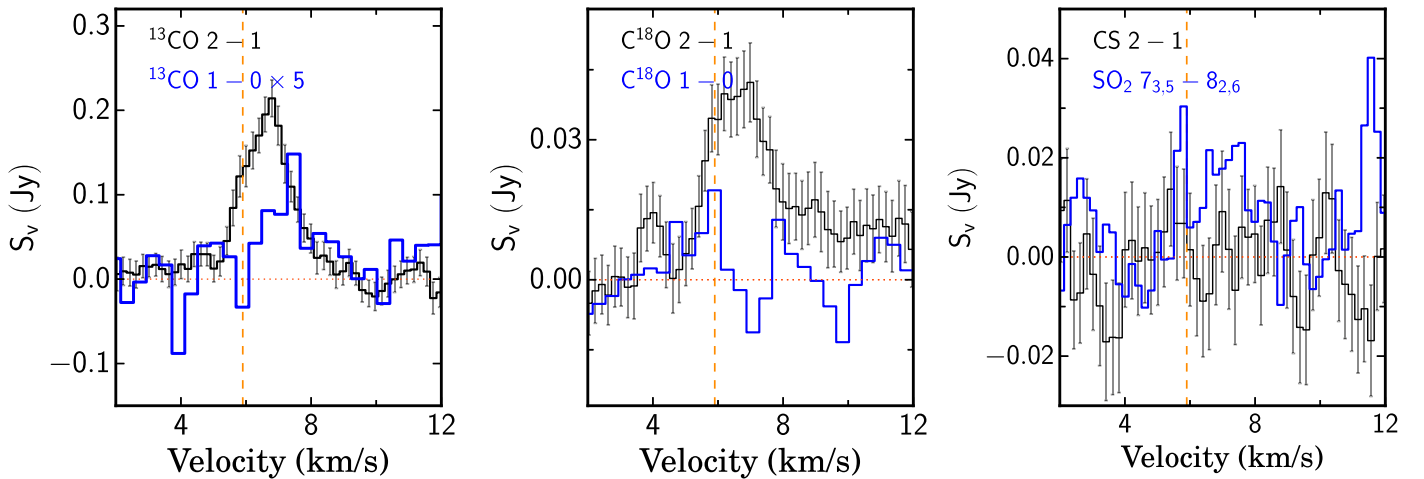
Figure 7. Molecular line profiles around CIDA 9A. As a reference, ^{13}CO and C^{18}O $J = 2$–1 are shown with black lines in the left and middle panels. Their $J = 1$–0 counterparts are shown in blue. In addition, CS 2–1 and SO2 $7_{3,5} - 8_{2,6}$ are plotted in the right panel. These spectral lines are extracted with *GoFish*, adopting the stellar and disk parameters of Rota et al. (2022).

associated with molecular winds. The moment maps of these lines can be found in Appendix B.

4. Discussion

Our high-spatial-resolution observations of the transitional disk around CIDA 9A in Band 3 show similar asymmetric substructures as the previous Band 6 data. In order to bring out the dust substructures, we have deconvolved the images with a $0\rlap{.}''09$ taper and a $0\rlap{.}''135$ circular beam. The aim is to find differences in the observed substructures between the Band 3 and 6 data. Our data indicate a speculative azimuthal shift in the location of the main dust emission peak between Bands 3 and 6 and an upper limit of 3 au radial shift characterized by a localized spectral index $\alpha < 3$. We will focus on discussing the main mechanisms that can form the transition disk around CIDA 9A.

A wide variety of mechanisms can be invoked to explain the large asymmetric disk with a cavity in the submillimeter around CIDA 9A. As shown by Long et al. (2018), CIDA 9A does not indicate a dust cavity through its spectral energy distribution. The major difference between CIDA 9A and other sources with known large asymmetric dust traps is the properties of the central star. Most of the previous detections of dust asymmetries are around Herbig and/or Sun-like stars, while there are only a few detections of an asymmetric dust ring around $<1\,M_\odot$ stars[16] (González-Ruilova et al. 2020; Hashimoto et al. 2021).

The millimeter cavity in CIDA 9A can be carved by either an embedded planet, disk wind, and/or dead zone. To favor between a vortex generated by an embedded planet and a dead zone, we are looking for potential radial and azimuthal differences between the Band 3 and 6 observations, although this does not provide a definitive answer about the origin of the cavity. In the case of a massive protoplanet (the mass depends on the disk viscosity and scale height), we expected a drop of gas and dust inside the millimeter cavity (e.g., Lubow & D'Angelo 2006; Zhu et al. 2011; Rosotti et al. 2013; Duffell & Dong 2015; Kanagawa et al. 2017; Villenave et al. 2019) and an azimuthal shift between small and dust grains due to the vortex (Baruteau & Zhu 2016). If disk wind is the main driver

of the cavity formation (Alexander & Armitage 2007; Rosotti et al. 2013; Ercolano & Pascucci 2017; Gárate et al. 2021), we expect a large gas-depleted cavity and the presence of broad molecular line emission as the gas is entrained from the millimeter cavity. Last, a pressure trap generated at the edge of the dead zone can form a cavity and a millimeter dust ring (Flock et al. 2015). Pinilla et al. (2019) showed a radial shift between small and large dust grains due to the pressure trap generated by a dead zone.

We step through several possible scenarios of how the observed millimeter could have been formed and discuss whether their observable signatures are observed.

Giant Protoplanet. Although most of the observed dust asymmetry is explained by protoplanets embedded in the disk or the gap, this explanation is not straightforward for CIDA 9A. Millimeter dust can be confined in a vortex near the dust gap or cavity formed by a Jupiter-type planet (Dong et al. 2015). The observed total emission from the disk around CIDA 9A is 30–40 mJy at 233 GHz, which translates to 0.18–0.25 $M_{\rm Jup}$ of solids, adopting a dust temperature of 20 K and a dust grain absorption opacity of 10 cm^2 g^{-1} at 1000 GHz, with a frequency dependence $\beta = 1$ (Beckwith et al. 1990). As mentioned earlier, the dust temperature at the dust ring's location is $\sim$25 K, which lowers the total dust mass. A giant planet could have formed when the disk was more massive in the first 1 Myr (e.g., Drazkowska et al. 2023 and references therein).

Rota et al. (2022) showed that gas is still present in the dust cavity of CIDA 9A. On the other hand, our high-spatial-resolution CO data observations do not have the spatial resolution and sensitivity to infer the underlying gas distribution for comparison with the dust distribution. Recently, Pinilla et al. (2021) and Hashimoto et al. (2021) have shown cavities that indicate the possible presence of giant planets around very low-mass stars. In comparison to CIDA 9A, the ZZ Tau IRS disk still has about 0.07–0.15 $M_{\rm jup}$ (0.18–0.25 $M_{\rm jup}$ for CIDA 9A) dust mass around it. With the revised higher stellar mass obtained for CIDA 9A, it is still possible that there is a protoplanet inside the millimeter cavity since the disk mass could be much higher in its earlier stages.

If a planet was present, in addition to the difference in gas and dust distributions, a gas vortex could form at the outer edge of the

---

[16] The adopted mass for this paper relies upon pre-main-sequence evolutionary tracks that produce higher masses. Many previous measurements of other disk-hosting stars rely on models that yield lower masses for the same parameters.
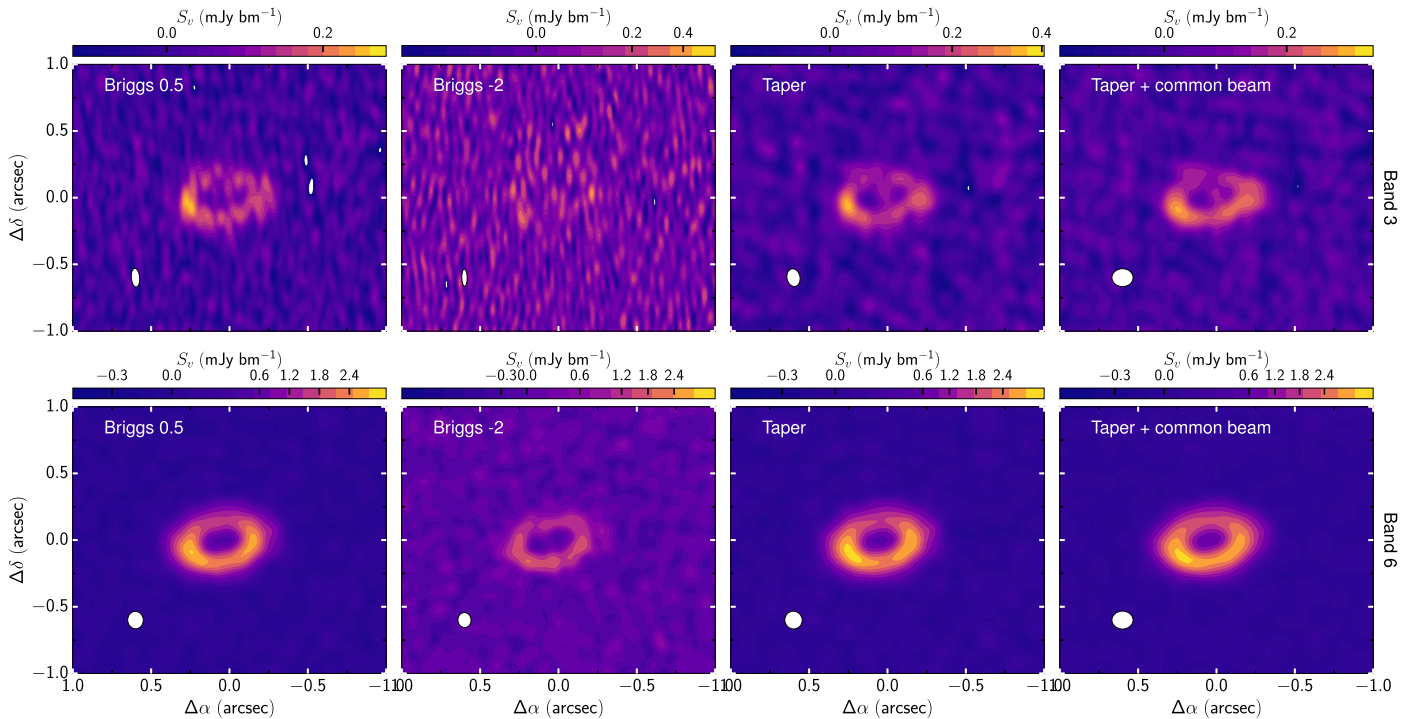
Figure 8. Dust continuum images of CIDA 9A. Top: Band 3 images. Bottom: Band 6 images. These images are cleaned with a Briggs weighting. The tapered images ("Taper") are constructed with a Briggs weighting of 0.5 and a tapering at $0\rlap{.}{''}08$. The panels that are indicated by "Taper + common beam" are images that are restored with a common beam of $0\rlap{.}{''}135$.

cavity (de Val-Borro et al. 2007; Ataiee et al. 2013; Pinilla et al. 2022). At the location of the ring of CIDA 9A, the orbital time is ~300 yr. Pinilla et al. (2022) found that the dust concentration inside such a vortex remains after 3000 orbits or 9×10^5 yr. Since CIDA 9 is likely 3–10 Myr old, it seems that the dust concentration should be maintained by other mechanisms. By considering realistic planet formation timescales, a double-peaked millimeter emission that is observed toward CIDA 9A can be obtained by a single vortex after long times of evolution (Hammer et al. 2019). The observed azimuthal shift is still consistent with this scenario.

The final observable signature of an embedded protoplanet is the spiral arms in the scattered light. Unfortunately, CIDA 9A is faint in the Two Micron All Sky Survey (2MASS)[17] and difficult to follow up with ground-based IR instruments. Therefore, we could not obtain any scattered-light images. At the moment, the suitable way to rule out the presence of a giant protoplanet is to obtain high-spatial-resolution and high-sensitivity CO isotopologue (^{12}CO, ^{13}CO, and C^{18}O) observations toward the millimeter cavity around CIDA 9A, to measure the underlying gas distribution with respect to the dust.

Winds. From the detection of CO gas emission inside the millimeter cavity, it places limits on how photoevaporation may form the millimeter cavity in CIDA 9A. On the other hand, our molecular line data are not sufficient to constrain the presence of any fast wind. It is not possible to constrain whether a wind is still actively driving the evolution of the millimeter cavity toward CIDA 9A without additional gas-line (atomic and molecular) observations to constrain the wind.

Dead Zone. Our results indicate a tentative azimuthal shift between the smaller dust grains as traced in Band 6 (~230 GHz,

1.3 mm) and the larger dust grains in Band 3 (~90 GHz, 3.1 mm). If the azimuthal shift is $\sim20°$, as shown by the (u, v) model, it is in agreement with the hydrodynamical simulations of gas and dust with a vortex in Baruteau & Zhu (2016), where larger grains (here traced with Band 3) are expected to be shifted ahead of the vortex in the azimuthal direction. If this is the case for CIDA 9A, this implies that the disk rotation is clockwise. As shown in Baruteau & Zhu (2016), such a shift can also produce a double-peaked azimuthal emission. The models from Baruteau & Zhu (2016) assume an initial perturbation in the gas density profile that triggers the vortex formation and that can have different origins, such as planets, photoevaporation, and dead zones. The current data do not seem to favor any of these origins. The dead-zone models presented by Pinilla et al. (2019) predict a radial shift of the millimeter emission at different wavelengths (the peak closer to longer), which is opposite to the prediction in the planet–disk interaction models. In CIDA 9A, there is an indication of a very small radial shift, but it is too small to give any firm conclusion on the cavity origin, based on these observations.

In order to investigate the processes that shape the disk around CIDA 9A, much deeper ALMA observations in multiple frequency bands are required. In addition, deeper molecular gas emission that targets the molecular wind and warm gas within the millimeter cavity are needed to constrain the role of photoevaporative wind in shaping the disk evolution. In particular, high-spatial-resolution Band 9 observations would help to completely rule out the presence of a vortex at the edge of the dead zone by constraining the radial shift between Bands 3, 6, and 9. The millimeter dust ring produced at the edge of a dead zone is predicted to show an optically thick emission from the small dust grains that are radially shifted with respect to the longer-wavelength emissions. Furthermore, a more detailed hydrodynamical evolution

---

[17] The faint near-IR photometry with 2MASS may be the consequence of a faint epoch or confusion between the primary and secondary. The source is probably brighter in most epochs.
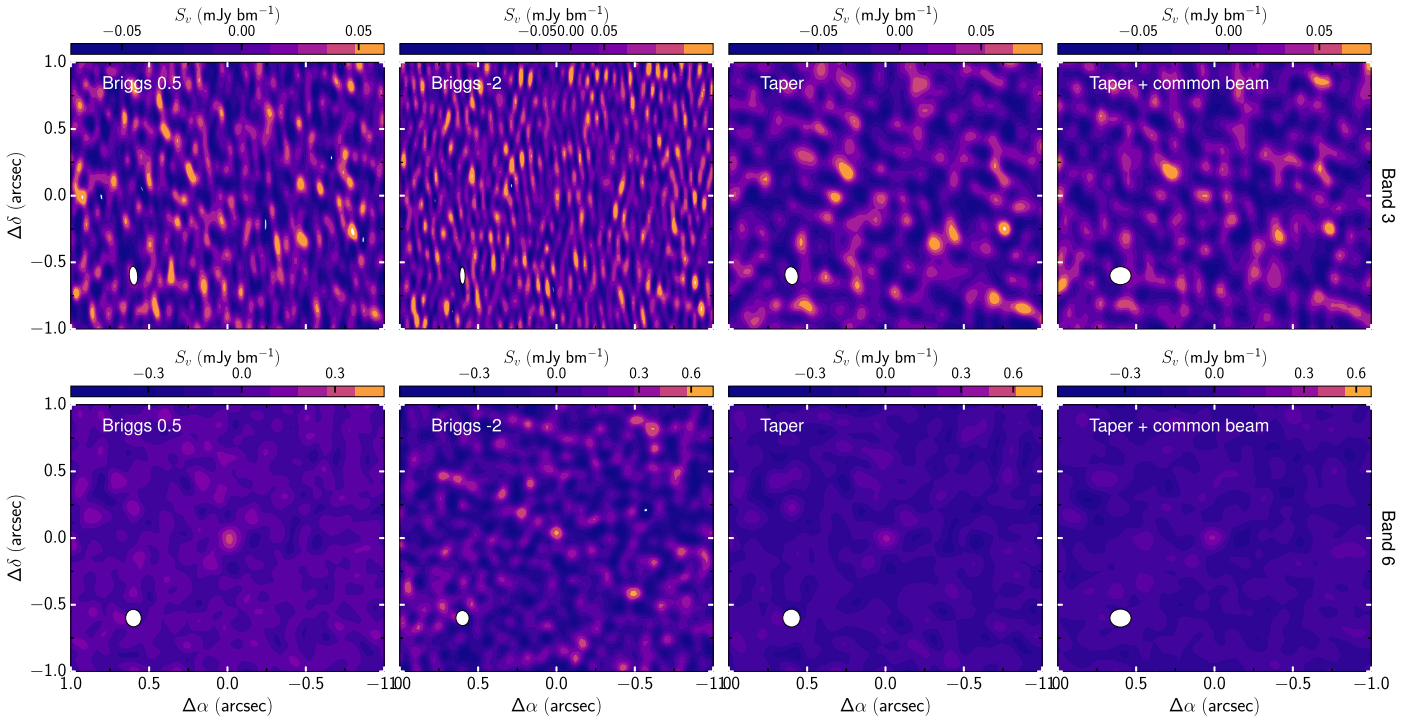
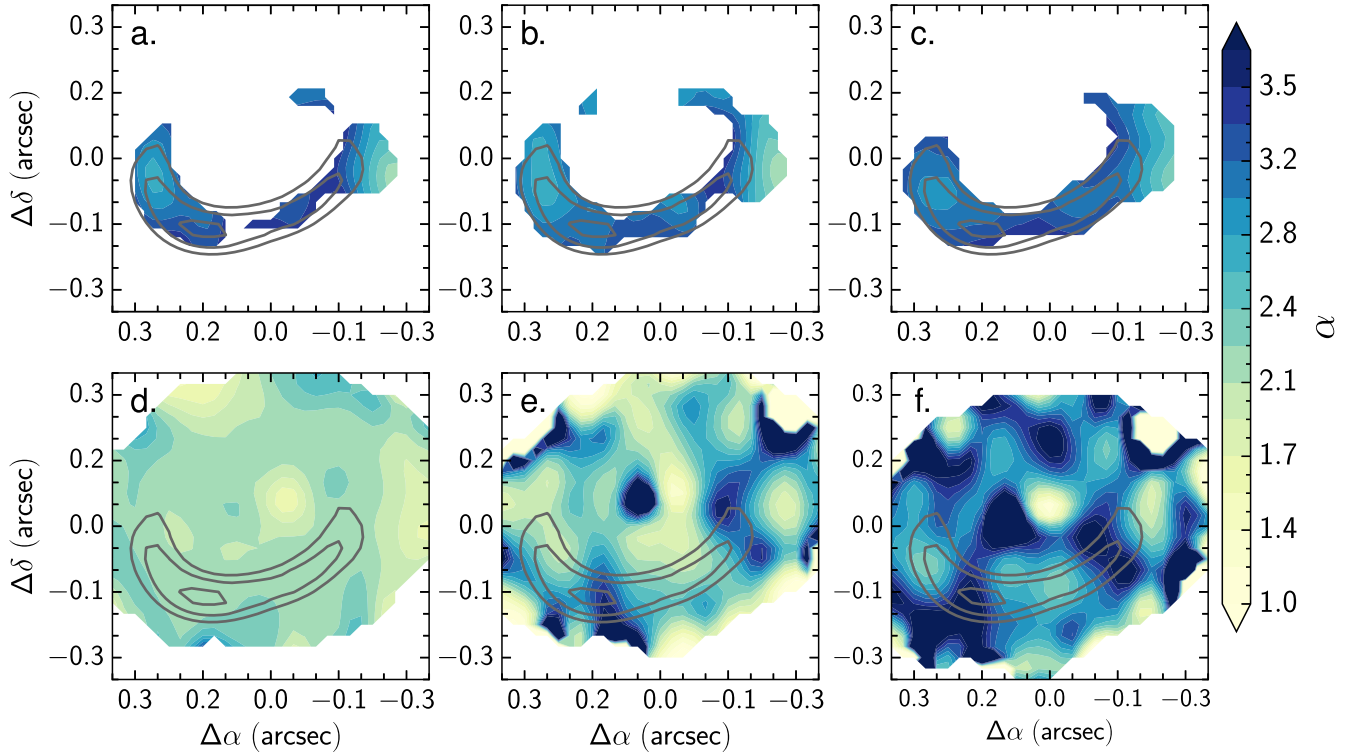**Figure 9.** Similar to Figure 8, but for CIDA 9B.

Figure 10. Spectral index maps of the primary disk. The top row (panels (a), (b), and (c)) shows the spectral index α as derived in the image plane. Panel (a) is the spectral index map of the dust continuum images constructed with a tapering at $0''\!\!.09$ with *mfs* and a Hogbom deconvolver. Panel (b) shows the map using MTMFS and a taper, while panel (c) shows the map in the case of the combination of tapering and a common beam of $0''\!\!.135$. The second row shows the spectral index map as produced by TCLEAN MTMFS. Panels (d), (e), and (f) show the α map with an increasing number of Taylor coefficients, from two to four. The gray contours indicate the dust continuum emission of the concatenated Band 3 and 6 visibilities at 35σ, 40σ, and 45σ.

of multiple mechanisms is needed to compare with these new observations of disks.

Spectral Index of CIDA 9A. The spectral index can be used as an observational diagnostic of dust growth when the millimeter emission is optically thin. In the case of CIDA 9A, a lower value of the spectral index in the radial direction is found along the main dust peak. The low spectral index between the two bands can also indicate a higher optical depth.

On the other hand, the observed spectral index $\alpha > 2$. The dust spectral index around the main dust peak is close to 3 outside the main dust peak, and the value gradually decreases toward the center of the main dust peak. This suggests that particles have grown to millimeter sizes at this location, as expected from a vortex (Birnstiel et al. 2013). The spectral index increases with distance from the main dust peak, as expected from dust evolution models and as has been observed in several protoplanetary disks (e.g., Pérez et al. 2012; Tazzari et al. 2016; Long et al. 2020) and in disks with clear asymmetric rings (Casassus et al. 2015; van der Marel et al. 2015).

For the western dust peak, the spectral index shows a slight decrease at this radial position, but it continues decreasing radially, suggesting that grains are large in the outer parts of the disks. Unlike its brighter counterpart, this secondary peak seems to be inconsistent with a vortex, because otherwise the large grains would have concentrated in the vortex and only small grains would remain outward (increasing the spectral index), as observed for the main dust peak. Multiwavelength observations of CIDA 9A at higher sensitivity and resolution are needed to confirm this unusual behavior of the spectral index.

5. Summary and Conclusions

Multiband observations of protoplanetary disks have been essential in constraining the physical mechanisms responsible for forming transition disks. The end stages of disks and how they disperse are crucial in understanding both disk evolution and planet formation. This paper presents Band 3 and 6 ALMA observations of the transition disk around an M dwarf, CIDA 9A. The main results and conclusions can be found below:

1. We detected an asymmetric disk that can be modeled as a Gaussian ring and two arcs in our Band 3 data. With a higher spatial resolution, the disk in Band 3 looks as asymmetric as in Band 6. The secondary disk CIDA 9B is not robustly detected in Band 3. The dust emission consists of the main dust concentration to the east or the main dust peak and the secondary dust peak to the west.

2. With the two frequencies, we find a localized dust spectral index that dips to $\alpha_{B3-B6} \sim 2.8$ at the main dust emission peak. The dust spectral index is calculated using the dust continuum images. The dust emission seems to be optically thin in Band 3, while it is marginally optically thick $\tau \gtrsim 0.3$ in Band 6. With these results, we cannot conclusively show that the large dust grains are concentrated at the dust emission peaks.

3. Both Bands 3 and 6 data have been analyzed in the (u, v) space by fitting the visibilities with an axisymmetric Gaussian ring model and a combination of a Gaussian ring and two Gaussian arcs (GR2ARC) model. These fits indicate that the dust emission peaks are not radially shifted with respect to each other. However, the models indicate a tentative azimuthal shift of $\sim 22^{+5}_{-36}{}^{\circ}$ between the peak position in Bands 3 and 6 that requires further investigation.

4. Our data also contain CO molecular lines, SO_2, and CS. We can recover the ^{13}CO and $C^{18}O$ $J = 1$–0 lines using velocity-based masking. On the other hand, the CS $J = 2$–1 and SO_2 lines are tentatively detected within the millimeter cavity. With these molecular data, we constrain the stellar mass to be around 0.62–0.72 $M_{\odot}$, adopting an inclination of $i \sim 47^{\circ} \pm 2^{\circ}$ as derived from the (u, v) model of the dust continuum data.

5. The tentative azimuthal shift of $\sim 22^{+5}_{-36}{}^{\circ}$ is consistent with a dust trap caused by a vortex. On the other hand, we cannot determine the cause of the vortex in the disk around CIDA 9A. Deeper observations in both the dust continuum and molecular lines are needed to investigate whether the vortex is generated by an unseen planet or other hydrodynamical instabilities.

Appendix A
Continuum Images

We have imaged both the Band 3 and 6 data separately with CASA TCLEAN. In order to analyze the two images in a consistent manner, we presented the results above based on

images that are deconvolved with a 0″09 taper and a common restoring beam. Figure 8 shows CIDA 9A as imaged using various deconvolution parameters, including Briggs weighting and the fixed restoring beam. The structures are similar within the different images.

The secondary star CIDA 9B is located 2″35 away to the direction of the northeast of the primary disk (Manara et al. 2019). The dust continuum emission in Band 6 from the disk around CIDA 9B is barely detected at a ∼3σ level with our imaging. Manara et al. (2019) reported a detection at 0.32 mJy in Band 6, which is at the 5σ level in a ∼0″14 × 0″11 beam. The secondary disk is shown in Figure 9, centered on the coordinates reported by Manara et al. (2019). As shown, CIDA 9B is detected in Band 6 (1.3 mm), but it is not clearly detected in Band 3 (3.1 mm). The upper limit in Band 3 is 31 μJy within a 0″135 beam and 23 μJy as determined from the image with a Briggs weighting of 0.5. The upper limit to the dust emission in Band 3 is 0.20 mJy within 0″1. With these flux densities, the lower limit to the spectral index of CIDA 9B is ∼3.4, with an error of 0.4 that takes into account a 20% flux error.

In the main part of this manuscript, we evaluated the dust spectral index profile using the images in Figure 1. For completeness, Figure 10 shows the complete dust spectral index maps evaluated using a different set of deconvolution parameters, including MTMFS. We use $\alpha = \frac{\Delta I}{\Delta \nu}$ to calculate the spectral index. Panels (a), (b), and (c) show the α map using the values that are derived from the images. The differences between panels (a), (b), and (c) are due to the different parameters that are adopted during deconvolution with TCLEAN. Panel (a) shows the result from deconvolution using *mfs* with a tapering at 0″09 and Hogbom deconvolution. Panels (b) and (c) use the MTMFS deconvolver while keeping the taper

at 0″09. The image in panel (c) is restored with a common beam of 0″135.

It is clear that the spectral index map is highly dependent on the adopted deconvolution options. The images that are produced with MTMFS using two Taylor terms tend to produce $\alpha \sim 2$, which is indicative of optically thick emission. This value is in strong contrast to $\alpha \sim 2.8$, which is the value obtained by deriving the spectral index from the images. The difference is very crucial in interpreting the grain size distribution around the dust continuum emission. $\alpha \sim 2$ indicates an optically thick emission, while $\alpha \sim 2.8$ is a moderate grain growth.

The major differences could be due to the fact that we are attempting to derive a spectral index using two frequencies. However, ALMA should provide high-quality data that can be used to derive the spectral index using the different spectral windows in Bands 3 and 6. Following Tsukagoshi et al. (2022), we tested a spectral index that is derived with MTMFS using a higher number of Taylor coefficients. We find that the indices that are obtained using three and four Taylor coefficients are more consistent with those values obtained in the image plane.

Appendix B
Moment Maps

Due to the low-S/N data on the targeted gas lines in Band 3, we did not include the moment maps in the main section of the paper. The moment maps of the Band 6 data have been published in Rota et al. (2022). Figure 11 shows the zeroth moment maps of the major species, while Figure 12 shows the moment maps constructed with the Keplerian masking. As explained in the results section, we adopted an inclination that was derived by fitting the dust continuum emission.
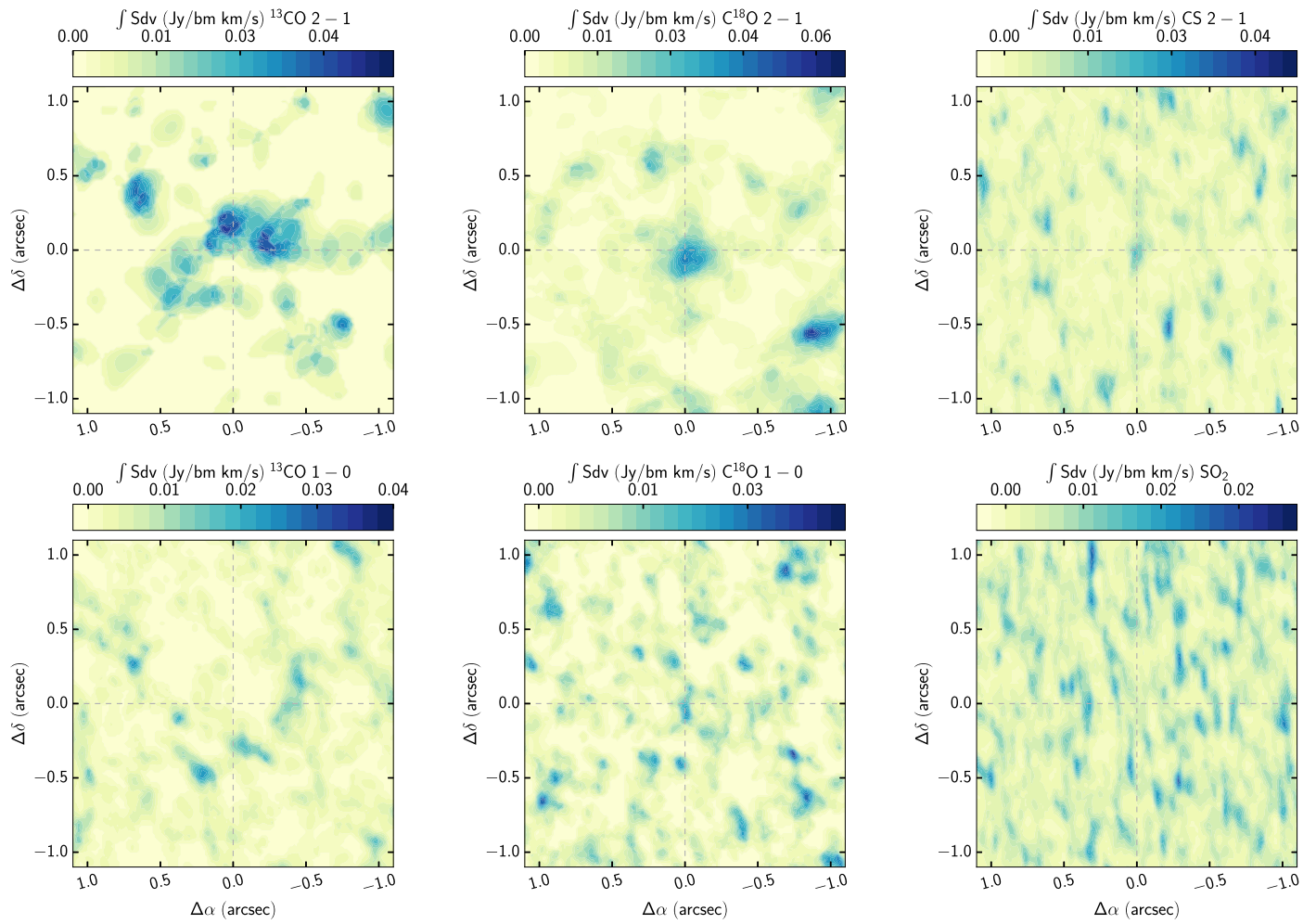
Figure 11. Integrated line maps (zeroth moment) of ^{13}CO $J = 2$–1, $C^{18}O$ $J = 2$–1, CS $J = 2$–1, ^{13}CO $J = 1$–0, $C^{18}O$ $J = 1$–0, and SO2 $7_{3,5} - 8_{2,6}$. The spectral cubes are integrated from 2 to 10 $km\,s^{-1}$. Only emissions above 2σ are considered.
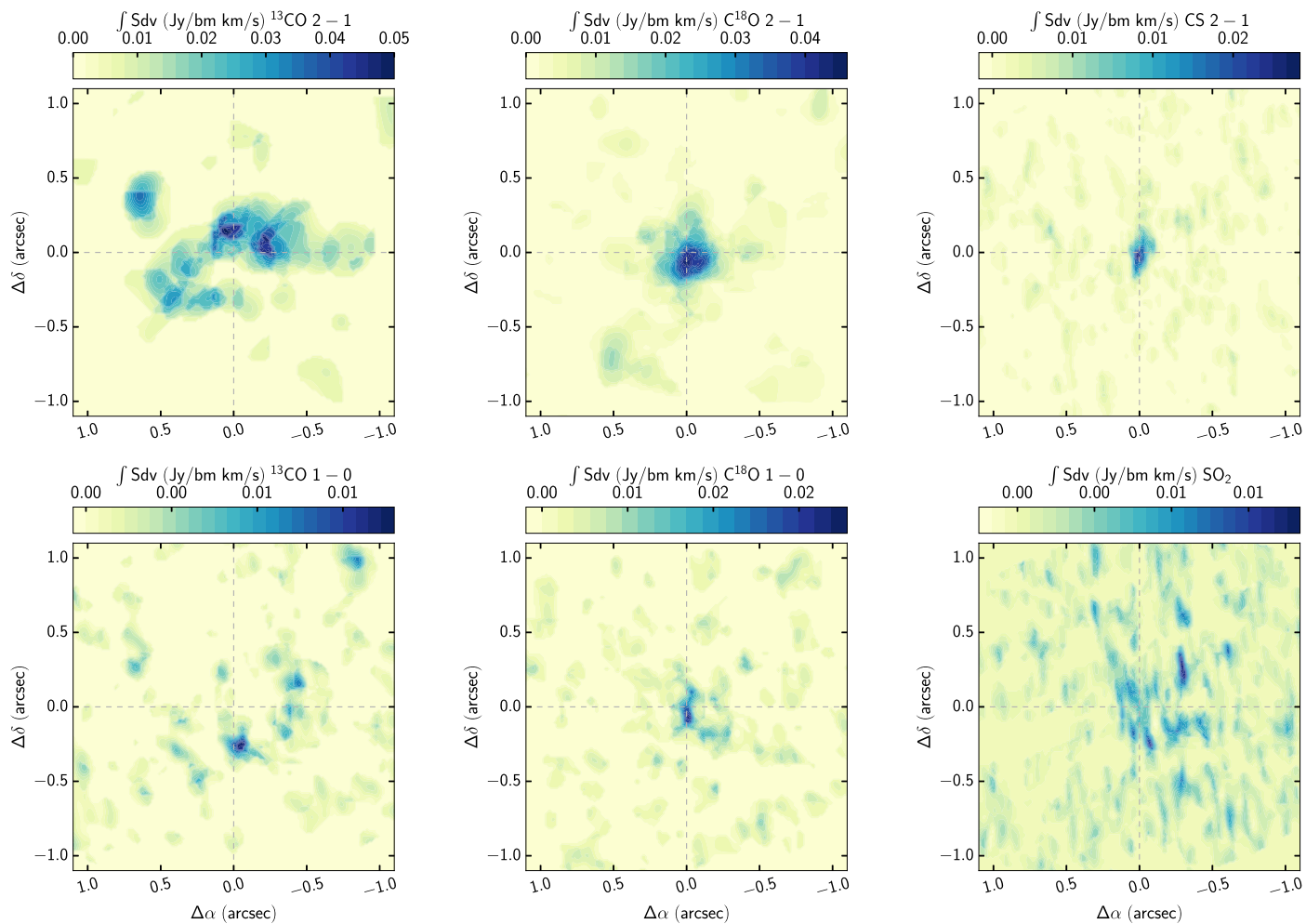
Figure 12. Similar to Figure 11, but with the addition of a velocity-based masking. We adopted $i = 47°$ and a stellar mass of $0.7 M_\odot$.

Appendix C
Results from the (u, v) Modeling

We have presented the results of the fits using the GR2ARC model in the main text. In particular, we have also used the axisymmetric Gaussian ring model to fit the observed substructures consistent with the results presented by Long et al. (2018). Figure 13 shows the results for the axisymmetric Gaussian ring model.
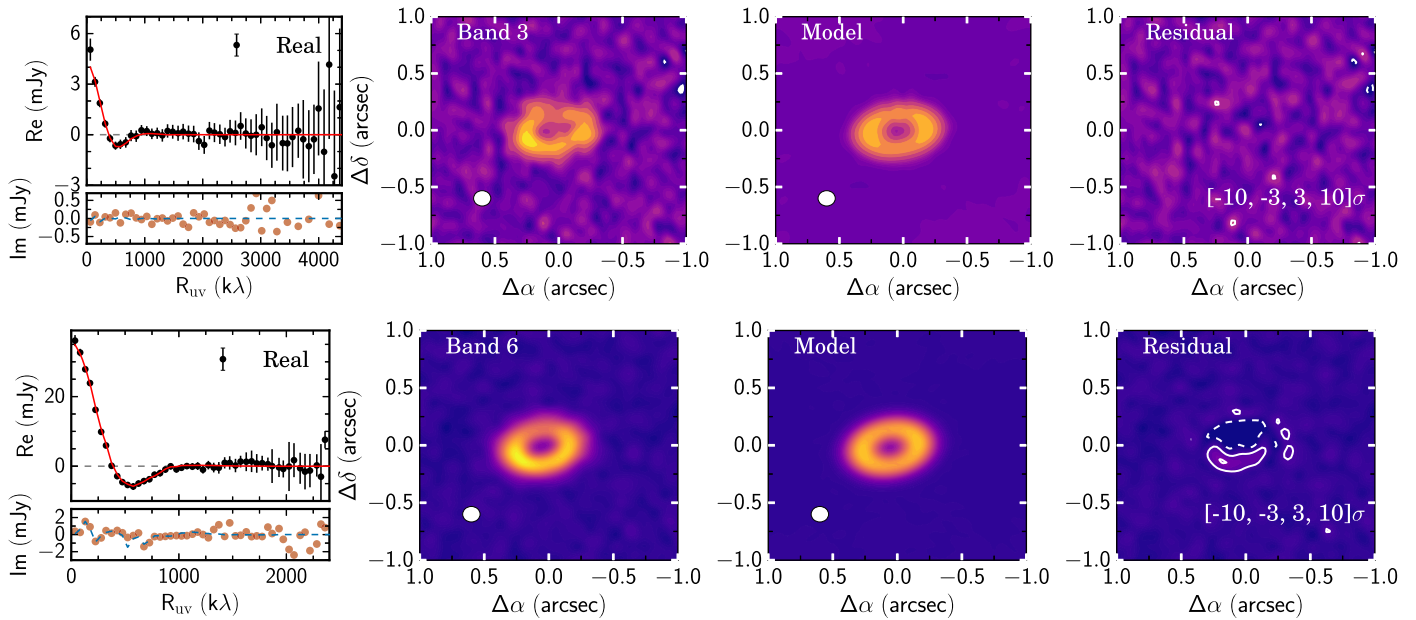
Figure 13. Best-fit models of the dust morphology in Bands 3 and 6. Top: the best-fit models for the Band 3 data. Bottom: the best-fit model for the Band 6 data. For each row, we show the binned visibilities, the original image, the model image, and the residual. For the residual image, the contours at -10σ, -3σ, 3σ, and 10σ are indicated by the white lines.

ORCID iDs

Daniel Harsono ⓘ https://orcid.org/0000-0001-6307-4195
Feng Long ⓘ https://orcid.org/0000-0002-7607-719X
Paola Pinilla ⓘ https://orcid.org/0000-0001-8764-1780
Carlo F. Manara ⓘ https://orcid.org/0000-0003-3562-262X
Gregory J. Herczeg ⓘ https://orcid.org/0000-0002-7154-6065
Doug Johnstone ⓘ https://orcid.org/0000-0002-6773-459X
Giovanni Rosotti ⓘ https://orcid.org/0000-0003-4853-5736
Giuseppe Lodato ⓘ https://orcid.org/0000-0002-2357-7692
Francois Menard ⓘ https://orcid.org/0000-0002-1637-7393
Marco Tazzari ⓘ https://orcid.org/0000-0003-3590-5814

References

Alexander, R. D., & Armitage, P. J. 2007, MNRAS, 375, 500
ALMA Partnership, Brogan, C. L., Pérez, L. M., et al. 2015, ApJL, 808, L3
Andrews, S. M., Huang, J., Pérez, L. M., et al. 2018, ApJL, 869, L41
Artymowicz, P., & Lubow, S. H. 1994, ApJ, 421, 651
Ataiee, S., Pinilla, P., Zsom, A., et al. 2013, A&A, 553, L3
Bae, J., Isella, A., Zhu, Z., et al. 2023, in ASP Conf. Ser. 534, Protostars and Planets VII, ed. S. Inutsuka et al. (San Francisco, CA: ASP), 423
Bae, J., Zhu, Z., & Hartmann, L. 2016, ApJ, 819, 134
Baraffe, I., Homeier, D., Allard, F., & Chabrier, G. 2015, A&A, 577, A42
Baruteau, C., & Zhu, Z. 2016, MNRAS, 458, 3927
Beckwith, S. V. W., Sargent, A. I., Chini, R. S., & Guesten, R. 1990, AJ, 99, 924
Benisty, M., Dominik, C., Follette, K., et al. 2023, in APS Conf. Ser. 534, Protostars and Planets VII, ed. S. Inutsuka et al. (San Francisco, CA: ASP), 605
Birnstiel, T., Dullemond, C. P., & Brauer, F. 2010, A&A, 513, A79
Birnstiel, T., Dullemond, C. P., & Pinilla, P. 2013, A&A, 550, L8
Boehler, Y., Ménard, F., Robert, C. M. T., et al. 2021, A&A, 650, A59
Boehler, Y., Ricci, L., Weaver, E., et al. 2018, ApJ, 853, 162
Booth, A. S., Tabone, B., Ilee, J. D., et al. 2021, ApJS, 257, 16
Briceno, C., Calvet, N., Gomez, M., et al. 1993, PASP, 105, 686
Briggs, D. S. 1995, AAS Meeting 187, 112.02
Calcino, J., Christiaens, V., Price, D. J., et al. 2020, MNRAS, 498, 639
Carrasco-González, C., Sierra, A., Flock, M., et al. 2019, ApJ, 883, 71
Casassus, S., van der Plas, G. M., Perez, S., et al. 2013, Natur, 493, 191
Casassus, S., Wright, C. M., Marino, S., et al. 2015, ApJ, 812, 126
Cazzoletti, P., van Dishoeck, E. F., Pinilla, P., et al. 2018, A&A, 619, A161

Chambers, K. C., Magnier, E. A., Metcalfe, N., et al. 2016, arXiv:1612.05560
Cieza, L. A., González-Ruilova, C., Hales, A. S., et al. 2021, MNRAS, 501, 2934
Currie, T., Lawson, K., Schneider, G., et al. 2022, NatAs, 6, 751
Delage, T. N., Okuzumi, S., Flock, M., Pinilla, P., & Dzyurkevich, N. 2022, A&A, 658, A97
de Val-Borro, M., Artymowicz, P., D'Angelo, G., & Peplinski, A. 2007, A&A, 471, 1043
Dong, R., & Fung, J. 2017, ApJ, 835, 38
Dong, R., Zhu, Z., & Whitney, B. 2015, ApJ, 809, 93
Drazkowska, J., Bitsch, B., Lambrechts, M., et al. 2023, in ASP Conf. Ser. 534, Protostars and Planets VII, ed. S. Inutsuka et al. (San Francisco, CA: ASP), 717
Duffell, P. C., & Dong, R. 2015, ApJ, 802, 42
Dullemond, C. P., & Dominik, C. 2004, A&A, 421, 1075
Endres, C. P., Schlemmer, S., Schilke, P., Stutzki, J., & Müller, H. S. 2016, JMoSp, 327, 95
Ercolano, B., & Pascucci, I. 2017, RSOS, 4, 170114
Espaillat, C., Muzerolle, J., Najita, J., et al. 2014, in Protostars and Planets VI, ed. H. Beuther et al. (Tucson, AZ: Univ. Arizona Press), 497
Fedele, D., Toci, C., Maud, L., & Lodato, G. 2021, A&A, 651, A90
Feiden, G. A. 2016, A&A, 593, A99
Flock, M., Ruge, J. P., Dzyurkevich, N., et al. 2015, A&A, 574, A68
Foreman-Mackey, D., Hogg, D. W., Lang, D., & Goodman, J. 2013, PASP, 125, 306
Francis, L., Johnstone, D., Herczeg, G., Hunter, T. R., & Harsono, D. 2020, AJ, 160, 270
Francis, L., & van der Marel, N. 2020, ApJ, 892, 111
Fung, J., & Chiang, E. 2016, ApJ, 832, 105
Gaia Collaboration, Brown, A. G. A., Vallenari, A., et al. 2018, A&A, 616, A1
Gaia Collaboration, Brown, A. G. A., Vallenari, A., et al. 2021, A&A, 649, A1
Galli, P. A. B., Loinard, L., Bouy, H., et al. 2019, A&A, 630, A137
Gárate, M., Delage, T. N., Stadler, J., et al. 2021, A&A, 655, A18
González-Ruilova, C., Cieza, L. A., Hales, A. S., et al. 2020, ApJL, 902, L33
Gully-Santiago, M. A., Herczeg, G. J., Czekala, I., et al. 2017, ApJ, 836, 200
Hammer, M., Pinilla, P., Kratter, K. M., & Lin, M. K. 2019, MNRAS, 482, 3609
Hammond, I., Christiaens, V., Price, D. J., et al. 2023, MNRAS, 522, L51
Hashimoto, J., Dong, R., & Muto, T. 2021, AJ, 161, 264
Herczeg, G. J., & Hillenbrand, L. A. 2008, ApJ, 681, 594
Herczeg, G. J., & Hillenbrand, L. A. 2014, ApJ, 786, 97
Huang, J., Andrews, S. M., Dullemond, C. P., et al. 2018, ApJL, 869, L42
Johansen, A., Oishi, J. S., Mac Low, M. M., et al. 2007, Natur, 448, 1022
Kanagawa, K. D., Tanaka, H., Muto, T., & Tanigawa, T. 2017, PASJ, 69, 97

Kenyon, S. J., & Hartmann, L. 1987, ApJ, 323, 714
Keppler, M., Benisty, M., Müller, A., et al. 2018, A&A, 617, A44
Klaassen, P. D., Juhasz, A., Mathews, G. S., et al. 2013, A&A, 555, A73
Klaassen, P. D., Mottram, J. C., Maud, L. T., & Juhasz, A. 2016, MNRAS, 460, 627
Klahr, H. H., & Henning, T. 1997, Icar, 128, 213
Kochanek, C. S., Shappee, B. J., Stanek, K. Z., et al. 2017, PASP, 129, 104502
Kraus, A. L., Herczeg, G. J., Rizzuto, A. C., et al. 2017, ApJ, 838, 150
Krolikowski, D. M., Kraus, A. L., & Rizzuto, A. C. 2021, AJ, 162, 110
Kurtovic, N. T., Pinilla, P., Long, F., et al. 2021, A&A, 645, A139
Lindegren, L., Hernández, J., Bombrun, A., et al. 2018, A&A, 616, A2
Liu, J., Fang, M., Tian, H., et al. 2021, ApJS, 254, 20
Liu, Y., Dipierro, G., Ragusa, E., et al. 2019, A&A, 622, A75
Long, F., Pinilla, P., Herczeg, G. J., et al. 2018, ApJ, 869, 17
Long, F., Pinilla, P., Herczeg, G. J., et al. 2020, ApJ, 898, 36
Lubow, S. H., & D'Angelo, G. 2006, ApJ, 641, 526
Luo, Y., Németh, P., Deng, L., & Han, Z. 2019, ApJ, 881, 7
Lyra, W., & Lin, M. K. 2013, ApJ, 775, 17
Manara, C. F., Tazzari, M., Long, F., et al. 2019, A&A, 628, A95
Matsuyama, I., Johnstone, D., & Murray, N. 2003, ApJL, 585, L143
McMullin, J. P., Waters, B., Schiebel, D., Young, W., & Golap, K. 2007, in ASP Conf. Ser. 376, Astronomical Data Analysis Software and Systems XVI, ed. R. A. Shaw, F. Hill, & D. J. Bell (San Francisco, CA: ASP), 127
Müller, A., Keppler, M., Henning, T., et al. 2018, A&A, 617, L2
Müller, H. S., Schlöder, F., Stutzki, J., & Winnewisser, G. 2005, JMoSt, 742, 215
Muro-Arena, G. A., Ginski, C., Dominik, C., et al. 2020, A&A, 636, L4
Paardekooper, S., Dong, R., Duffell, P., et al. 2023, in ASP Conf. Ser. 534, Protostars and Planets VII, ed. S. Inutsuka et al. (San Francisco, CA: ASP), 685
Pascucci, I., Sterzik, M., Alexander, R. D., et al. 2011, ApJ, 736, 13
Pecaut, M. J., & Mamajek, E. E. 2013, ApJS, 208, 9
Pérez, L. M., Carpenter, J. M., Chandler, C. J., et al. 2012, ApJL, 760, L17
Pickett, H. M., Poynter, R. L., Cohen, E. A., et al. 1998, JQSRT, 60, 883
Pinilla, P., Benisty, M., & Birnstiel, T. 2012, A&A, 545, A81
Pinilla, P., Benisty, M., Cazzoletti, P., et al. 2019, ApJ, 878, 16
Pinilla, P., Benisty, M., Kurtovic, N. T., et al. 2022, A&A, 665, A128
Pinilla, P., Flock, M., Ovelar, M. d. J., & Birnstiel, T. 2016, A&A, 596, A81
Pinilla, P., Kurtovic, N. T., Benisty, M., et al. 2021, A&A, 649, A122
Pinilla, P., Natta, A., Manara, C. F., et al. 2018, A&A, 615, A95
Remijan, A. J., & Markwick-Kemper, A. 2007, AAS Meeting 211, 132.11
Rosotti, G. P., Ercolano, B., Owen, J. E., & Armitage, P. J. 2013, MNRAS, 430, 1392
Rota, A. A., Manara, C. F., Miotello, A., et al. 2022, A&A, 662, A121
Shappee, B. J., Prieto, J. L., Grupe, D., et al. 2014, ApJ, 788, 48
Soderblom, D. R., Hillenbrand, L. A., Jeffries, R. D., Mamajek, E. E., & Naylor, T. 2014, in Protostars and Planets VI, ed. H. Beuther et al. (Tucson, AZ: Univ. Arizona Press), 219
Somers, G., Cao, L., & Pinsonneault, M. H. 2020, ApJ, 891, 29
Stadler, J., Benisty, M., Izquierdo, A., et al. 2023, A&A, 670, L1
Suzuki, T. K., & Muto, T. 2010, ApJ, 718, 1289
Tang, Y. W., Guilloteau, S., Piétu, V., et al. 2012, A&A, 547, A84
Tazzari, M., Beaujean, F., & Testi, L. 2018, MNRAS, 476, 4527
Tazzari, M., Testi, L., Ercolano, B., et al. 2016, A&A, 588, A53
Teague, R. 2019, JOSS, 4, 1220
Teague, R. 2019, JOSS, 4, 1632
Teague, R., & Foreman-Mackey, D. 2018, RNAAS, 2, 173
Testi, L., Birnstiel, T., Ricci, L., et al. 2014, in Protostars and Planets VI, ed. H. Beuther et al. (Tucson, AZ: Univ. Arizona Press), 339
The Astropy Collaboration, Price-Whelan, A. M., Sipőcz, B. M., et al. 2018, AJ, 156, 123
Tsukagoshi, T., Nomura, H., Muto, T., et al. 2022, ApJ, 928, 49
van der Marel, N., Birnstiel, T., Garufi, A., et al. 2021, AJ, 161, 33
van der Marel, N., Pinilla, P., Tobin, J., et al. 2015, ApJL, 810, L7
van der Marel, N., van Dishoeck, E. F., Bruderer, S., et al. 2013, Sci, 340, 1199
van der Marel, N., van Dishoeck, E. F., Bruderer, S., et al. 2016, A&A, 585, A58
Villenave, M., Benisty, M., Dent, W. R. F., et al. 2019, A&A, 624, A7
Weidenschilling, S. J. 1977, Ap&SS, 51, 153
Youdin, A. N., & Goodman, J. 2005, ApJ, 620, 459
Zhou, X., Herczeg, G. J., Liu, Y., Fang, M., & Kuhn, M. 2022, ApJ, 933, 77
Zhu, Z., Nelson, R. P., Hartmann, L., Espaillat, C., & Calvet, N. 2011, ApJ, 729, 47